

CONFERENCES AND SYMPOSIA

PACS numbers: **95.30.–k**, 97.60.Bw, 98.70.Sa

Astrophysical objects with extreme energy release: observations and theory

A M Bykov

DOI: https://doi.org/10.3367/UFNe.2017.04.038283

Contents

Abstract. **Supernovae release extreme amounts of energy and produce major chemical elements in galaxies. They are extraordinary phenomena that give rise to the emission of neutrinos, gravitational waves, and broad spectra of electromagnetic radiation, and accelerate particles to ultra-relativistic energies. Observations of supernovae have led to the discovery of the accelerated expansion of the Universe and the introduction of the 'dark energy' concept. Recent observations and theoretical models have revealed diverse supernova-related phenomena, the diversity resulting from variations both in the energy release mechanisms and in the properties of circumstellar matter. Supernova remnants and, in particular, gamma-ray bursts originating from compact stellar remnants are among the main objects of space research programs all over the world. We review the results of supernova and gamma-ray burst observations, as well as physical models capable of explaining the acceleration of nonthermal particles to ultra-relativistic energies and the amplification of fluctuating magnetic fields in supernova shells. We also consider the prospects of testing these models via observations with orbital and ground-based telescopes.**

Keywords: supernova, gamma-ray burst, shock wave, particle acceleration, cosmic rays

A M Bykov Ioffe Institute, Russian Academy of Sciences,
ul. Politekhnicheskaya 26, 194021 St. Petersburg, Russian Federation
E-mail: byk@astro.ioffe.ru

Received 21 January 2018
Uspekhi Fizicheskikh Nauk **188** (8) 894 – 908 (2018)
DOI: https://doi.org/10.3367/UFNr.2017.04.038283
Translated by K A Postnov; edited by A M Semikhatov

1. Introduction

Supernovae are objects with an extreme energy release that produce the main chemical elements in galaxies. These grandiose phenomena are accompanied by emission in a broad electromagnetic spectrum, neutrinos, gravitational waves, and the acceleration of nuclei to ultrarelativistic energies. Presently, observations of type-Ia supernovae (SNe) offer the possibility of probing the accelerated expansion of the Universe (see, e.g., [1]). The importance of SNe in the fundamental problem of searching for and determining the dark energy fraction in the Universe has led to unprecedented efforts to increase the observational SN statistics in several projects, including the Palomar Transient Factory, Dark Energy Survey, and Mobile Astronomical Network of Robotic Telescopes (MASTER). The Large Synoptic Survey Telescope (LSST) currently under construction should in five years be able to detect several thousand type-Ia SNe at redshifts of about one, as well as to study weak gravitational lensing effects. The LSST will also detect many thousands of transients (variable sources with a sharply increasing flux phase) each night. In the last decade, a significant increase in the statistics and quality of multiwavelength observations of SNe and other transients has enabled great progress in the understanding of the phenomenology and physics of SNe. Modern observations and theoretical models suggest a rich variety of observational manifestations of SNe caused by processes of energy release and different properties of circumstellar matter. Supernova remnants and gamma-ray bursts related to compact stellar remnants are in the focus of space research all over the world. In this paper, we briefly present the results of SN observations, gamma-ray bursts, and transients, including those related to the tidal disruption of stars. We discuss physical models of nonthermal processes in SN shells and prospects of probing them with next-generation orbital and ground-based telescopes.

The observational manifestations of SNe are very rich [2–4], a fact related to both different mechanisms of the huge energy release initiating an SN explosion and different progenitor stars that also determine the peculiarities of the circumstellar medium. The huge amount of observational data and large number of theoretical models force us to focus only on some issues related to nonthermal processes in SNe and their remnants. We consider classes of objects related to collapsing type-Ibc Sns, which are apparently related to recently discovered relativistic SNe. Physical processes in core-collapse SNe are discussed from the standpoint of the classical physics of shocks [5, 6], accretion theory [7], cosmic-ray physics [8], and the rapidly developing models of the formation and dynamics of collimated outflows from compact relativistic collapsars and cosmic particle accelerators.

2. Shocks in supernova shells

The dynamics of a shock in the upper atmosphere or a star strongly depend on the type of the star and its evolution before the SN explosion. This makes it possible to probe the stellar structure using observed emission spectra [9, 11]. After the core collapse, the shock propagates across the star almost adiabatically. The pressure downstream from the shock front is mainly determined by radiation, and photons with a mean free path Λ can reach the distance $c\Lambda/v_{\rm sh}$ upstream from the shock, where $v_{\rm sh}$ is the shock velocity. The breakout of a shock with high radiation energy density behind the front from an optically thick medium in the first minute is expected to be accompanied by a short and powerful ultraviolet (UV) and X-ray flash with a luminosity reaching 10^{45} erg s^{-1}. After this burst, more prolonged intensive UV and optical emission from the cooling plasma behind the shock should follow (see review [11]).

Observations of a very short UV–X-ray flash due to the shock breakout from an optically thick medium represent a significant issue and are yet to be confirmed. At the same time, many observations of the radio, optical, and X-ray light curves on longer time scales are described very successfully by numerical and analytic models of shock propagation through external stellar layers and the circumstellar medium [4, 12, 13]. The motion of a spherical shock and rarefication shock across the stellar layers with an inhomogeneous density distribution is accompanied by shock front deceleration in the inner low-density gradient regions. On the other hand, in the upper layers of the stellar envelope with a sharp density decrease, the shock front accelerates [14–20].

Thus, depending on the density distribution in the upper stellar layers, a kinetic energy distribution of the SN shell over the ejected matter velocity is formed. The outer parts of the shell can be accelerated to relativistic velocities. The relativistic acceleration of the SN shells is most effective in stars with radiative envelopes shining with a luminosity close to the Eddington limit [20]. Numerical calculations and an approximate expression for the kinetic energy $E_{\rm k}(>\Gamma_{\rm f}\beta_{\rm f})$ of the fraction of the shell matter propagating with the four-velocity $\Gamma\beta$ above a certain value $\Gamma_{\rm f}\beta_{\rm f}$ are given in [20]. For the density profile outside the stellar core, $r_{\rm c} < r < R$,

$$\rho(r) = \rho_{\rm h}\left(\frac{R}{r} - 1\right)^n ,$$

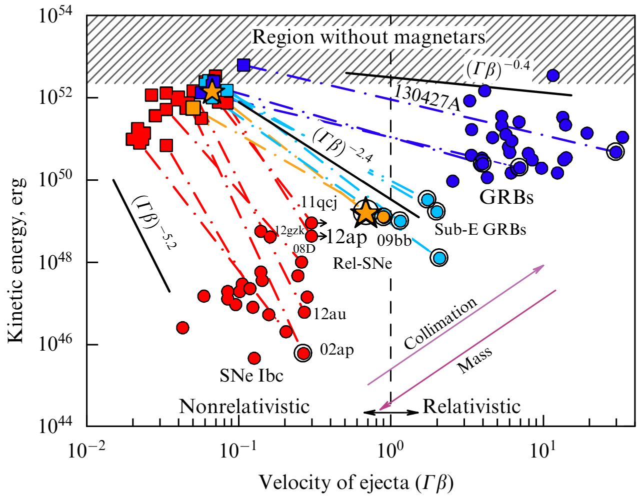

Figure 1. (Color online.) Population of sources with a different distribution of the kinetic energy on the ejecta four-velocity for three types of objects related to collapsing supernovae. Profiles of the spatial component of the ejecta four-velocity for the main Ibc supernovae (SNe Ibc) with nonrelativistic ejecta are shown in red; profiles for gamma-ray burst sources (GRBs) with ultrarelativistic jets are shown in blue. The intermediate ejecta profiles (so far scarce due to difficult observations) are shown in orange (relativistic supernovae (Rel-SNe) SN 2009bb and SN 2012ap without a gamma-ray burst) and in blue (sub-energetic (Sub-E) gamma-ray bursts). (From paper [21].)

the asymptotic formula for the energy distribution of nonrelativistic velocities of the ejecta is

$$E_{\rm k}(>\Gamma_{\rm f}\beta_{\rm f}) \propto (\Gamma_{\rm f}\beta_{\rm f})^{-(5{,}35\gamma_{\rm p}-2)}, \quad \Gamma_{\rm f}\beta_{\rm f} \ll 1\,, \tag{1}$$

whereas for the relativistic ejecta, $\Gamma_{\rm f}\beta_{\rm f} \gg 1$, the kinetic energy distribution is flatter:

$$E_{\rm k}(>\Gamma_{\rm f}\beta_{\rm f}) \propto (\Gamma_{\rm f}\beta_{\rm f})^{-(1.58\gamma_{\rm p}-1)}, \tag{2}$$

where $\gamma_{\rm p} = (1 + 1/n)$ [20].

Figure 1, taken from [21], shows (red symbols) the result of observations of some type-Ibc SNe demonstrating good agreement with formula (1) for $n \approx 3$. Statistically, type-Ibc SNe constitute about 19% of all SNe [22]. Models of the shock breakout into the circumstellar medium with account of the contribution of emission from radioactive ^{56}Ni synthesized during the shock propagation enable a quantitative description of the observed light curves of many collapsing stars [4, 12, 13]. However, some aspects of the shock formation during the collapse of massive stars remain an open issue. Models have been developed in which the neutrino flux from the collapsing core initiates a shock propagating outwards into the stellar envelope.

Modern models take General Relativity (GR) effects, neutrino transfer, deviations from spherical symmetry, instabilities, and turbulence into account [23–27]. On the other hand, long gamma-ray bursts (shown in Fig. 1 in purple), whose origin is related to the core collapses of massive stars [28, 29], require a very flat energy distribution over the ejecta velocities. Models of shock acceleration in the outer parts of the SN shell with a sharp density decrease do not reproduce the required amount of kinetic energy of the relativistic ejecta. In alternative models of gamma-ray bursts and relativistic SNe [30–32], the strong magnetic field of the collapsar is the dominant energy source of the burst and provides the collimation of the relativistic outflow (see Section 7 below).

3. Nonthermal processes in supernovae. Magnetic fields of massive stars and supernovae

When an SN shock transits from the collisional regime to a collisionless one, nonthermal components with a significant energy density can be formed. The matter density $\rho_{\rm b}$ at the shock breakout with a velocity $v_{\rm sh}$ is related to the breakout radius as

$$\rho_{\rm b} \sim \frac{c m_{\rm p}}{v_{\rm sh}\sigma_{\rm T} R_{\rm b}}\,, \qquad (3)$$

where $\sigma_{\rm T}$ is the Thomson cross section and $m_{\rm p}$ is the proton mass [33]. For the radius $R_{\rm b} \sim 10^{14}$ cm, the rate of Coulomb collisions of protons at the shock front in the breakout region is $\nu_{\rm Coul} \approx 0.02\, v_9^{-4} R_{14}^{-1}$ [s^{-1}], much smaller than both the ion plasma frequency in this region $\omega_{\rm p} = (4\pi\rho c^2/m_{\rm p}^2)^{1/2} \sim 10^9\, v_9^{-1/2} R_{14}^{-1/2}$ [s^{-1}] and the ion cyclotron frequency $\omega_B \sim 6 \times 10^3 B$ [s^{-1}], if the magnetic field B in the shell exceeds 1 mG. These estimates suggest that after the shock breakout, the shock becomes collisionless at distances of the order of several dozen radii of a blue supergiant progenitor star or a few radii of a red giant. In Section 5, more detailed models of the structure of collisionless shocks in a rarefied plasma are considered.

The propagation of a collisionless shock and the efficiency of the energetic particle acceleration in the circumstellar medium of collapsing massive stars are determined by the mass-loss rate and stellar wind properties, as well as by the magnetic fields at different stages of the progenitor star evolution.

Magnetic fields on the surface of hot massive stars — core-collapse SN progenitors — play a significant role in the dynamics of the intensive stellar winds accelerated by the radiation of a hot star [34], and the large-scale (dipole) components also determine the field magnitude in the extended stellar wind region across which the SN shock wave propagates. Observations of magnetic fields in stars of early O and B spectral classes are very complicated. To determine the strength of large-scale (in particular, dipole) magnetic fields in hot star atmospheres, sensitive spectropolarimeters are used, enabling an estimate of the magnetic field from observations of the circular polarization and Zeeman splitting of spectral lines. The extensive observational program in [35] included the analysis of 4800 spectra with circular polarization from 560 O and B stars in a wide range of masses, temperatures, and rotational velocities. Seven percent of the stars from this set revealed the presence of large-scale magnetic fields with a strength ranging from 50 G to several kiloGauss.

Observations of the M-giant Betelgeuse (α Ori, HD39801) by the Narval spectropolarimeter [36] enabled the measurement of a significant circular polarization (Stokes parameter V). The corresponding large-scale magnetic field (averaged over the stellar surface) is of the order of 1 G. Recent high-precision observations of the ^{28}SiO line by the ALMA (Atacama Large Millimeter Array) telescope enabled estimating the equatorial rotational velocity, which turned out to be rather low: $V_{\rm eq} \sin i = 5.47 \pm 0.25$ km s^{-1} [37]. The Betelgeuse red giant with the mass $\gtrsim 15\, M_\odot$ and radius of around 1000 solar radii is of special interest because it can explode as a type-IIP or type-IIL SN with a high probability in the near future. Observational data on the structure of the magnetic field in stellar winds of massive stars are quite scarce so far [38]. Magnetohydrodynamic (MHD) modeling [34] describes the field structure in the anisotropic wind formation zone at distances of about several stellar radii. Modeling particle acceleration during SN shock propagation in the progenitor star wind [39] typically assumes a simplified magnetic field configuration with the asymptotic dominance at large distances of a slowly decreasing tangential field caused by stellar rotation.

Estimates of the magnetic field in SNe and their remnants can be obtained from observations of radio emission detected during the first months after an explosion from several dozen collapsing SNe. The radio spectra of collapsing type-II and type-Ibc SNe are very different. For example, type-Ibc SN 1994I demonstrates the radio spectral index $\alpha \sim 1.22$, while the bright type-IIb SN 1993J has $\alpha \sim 0.81$ [40]. Also different is the time evolution of the brightness temperature of these SNe. The mass-loss rate from the putative Wolf–Rayet progenitor of SN 1994I, as derived from observations, is $\dot M \gtrsim 10^{-4} M_\odot$ yr^{-1}, while for SN 1993J, $\dot M < 10^{-5} M_\odot$ yr^{-1} [40]. The origin of SN 1993J is thought to be related to the explosion of a 15–20 $M_\odot$ supergiant that lost its hydrogen envelope in a close binary system with a comparable-mass companion. The magnetic field estimated from radio observations is about 2 G for SN 1993J (for the shock radius 1.6×10^{16} cm) and 2 G for SN 1994I (for the shock radius 3×10^{15} cm). There are grounds to believe that in type-Ibc SNe, the radio emission is confined within a thin layer near the external shock, whereas in type-II SNe with shells mixed due to Rayleigh–Taylor instabilities, the radio emission region is much broader [41].

Radio light curves frequently exhibit an increasing radio flux with a subsequent power-law time decrease. To estimate the magnetic fields from radio light curves of SNe, the low-frequency absorption mechanism has to be specified. The free–free optical depth $\tau_{\rm ff}$ in the stellar wind plasma with a velocity $V_{\rm w}$ depends on the wind characteristics: $\tau_{\rm ff} \propto (\dot M/V_{\rm w})^2 R^{-3} \nu^{-2.1}$, which makes it substantial for stars with powerful mass loss and low-velocity wind, typical of type-II SN progenitors. In addition, synchrotron self-absorption can dominate in the formation of radio spectra from collapsing SNe in the case of fast rarefied stellar winds from Wolf–Rayet stars [42]. For the synchrotron self-absorption, the radio flux at a frequency ν in the optically thick part of the spectrum is $F_\nu \propto R^2 B^{-1/2} \nu^{5/2}$, whereas in the optically thin part, $F_\nu \propto R^3 N_0 B^{(s+1)/2} \nu^{-(s-1)/2}$. Here, a power-law energy distribution of relativistic electrons is assumed ($\propto N_0 \gamma^{-s}$ is the Lorentz factor for electrons). For radio SNe dominated by synchrotron self-absorption, the analysis of radio spectra enables estimating the emitting region radius R at the moment of maximum radio emission.

An analysis of the observed type-Ibc SNe likely produced by Wolf–Rayet stars suggests the need for an efficient magnetic field amplification behind the shock front with a field energy density $\varepsilon_{\rm B} \sim 0.1$ times that of the plasma behind the shock wave front [43]. Here, the X-ray emission, also of nonthermal origin, is due to the inverse Compton scattering of the emission by relativistic electrons. In Section 4, we discuss observations of magnetic fields from the interesting class of SNe with relativistic ejecta, and in Section 5 we consider the magnetic field amplification in SNe.

4. Relativistic supernovae

The rich variety of SNe includes a relatively rare group of objects demonstrating properties intermediate between most collapsing SNe and sources of gamma-ray bursts. This group is characterized by relativistic velocities of ejecta. Usually, these SNe demonstrate light curves and spectra typical of collapsing type-Ibc SNe but have a relativistic outflow leading, in particular, to an anomalously high radio luminosity during the first year after the explosion.

Type-Ibc SN 2009bb belongs to this class, having no associated gamma-ray burst but having a relativistic, possibly baryonic, matter outflow [21, 44]. SN 2009bb showed an unusually high radio luminosity for a SN of this type and a spectrum typical of synchrotron self-absorption with a relatively low spectral peak frequency. In the first radio observation at the frequency of 6 GHz, approximately 20 days after the explosion, a luminosity of 3.6×10^{28} erg s^{-1} Hz^{-1} was measured. This is more than an order of magnitude higher than radio luminosities of typical type-Ibc SNe, but is comparable to that of gamma-ray burst afterglows at the corresponding phase. The synchrotron self-absorption model enabled determining the shock radius $R \approx 4.4 \times 10^{16}$ cm, the relativistic shock velocity with the Lorentz factor $\Gamma_{\rm sh} \gtrsim 1.3$, and the energy of the relativistic outflow $E = (1.3 \pm 0.1) \times 10^{49}$ erg at the moment of the first radio observation [44].

The possibility of relativistic acceleration of a small fraction of baryonic matter during the time the shock crossed the outermost layers of the exploded star with a steeply decreasing density was discussed in Section 2. However, Eqns (1) and (2) obtained in [20] simultaneously predict an anomalously high energy of the nonrelativistic part of the ejecta (see Fig. 1). Therefore, a collimated energy ejection from the central compact object can be the possible source of the ejecta energy in relativistic SNe. In particular, the SN ejecta velocity distribution with account of the relativistic jets from the central compact source of various durations (4.0, 7.5, and 15.0 s) for the same total jet energy of 3×10^{51} erg was modeled in [31]. These calculations demonstrate the absence of a significant energy fraction in the SN ejecta with $\beta\Gamma \gtrsim 0.3$ for a jet duration of 4.0 s; in this case, the observational appearances can hardly be distinguished from the characteristic model properties of the hydrodynamic collapse of a type-Ibc SN. At the same time, the source activity over 7.5 s provides a flat energy distribution of the ejecta four-velocity up to $\beta\Gamma \gtrsim 1$, in agreement with the expected distribution in SN 2009bb. The central source activity over 15.0 s extends the flat energy distribution to $\beta\Gamma \gtrsim 100$, typical of gamma-ray burst models. The possible mechanisms of the prolonged activity of the central source include accretion onto the rotating compact object and millisecond magnetars. For example, some observational features of the bright SN 2011kl associated with the ultra-long gamma-ray burst GRB111209A can be explained by the magnetar model [45].

Relativistic radio-emitting ejecta were earlier discovered in the type-Ibc SN 1998bw and, in contrast to the ejecta in SN 2009bb, they were associated with the gamma-ray burst GRB 980425 [46, 47]. The radio flux from SN 1998bw decayed with time much faster than that from SN 2009bb. Observations of type-Ic SN 2012ap revealed the presence of mildly relativistic ejecta not associated with an observed gamma-ray burst but with a significantly shorter deceleration time than in SN 2009bb [48]. The deceleration of ejecta in the circumbinary medium is characterized by a power-law exponent m of the expansion of the external shock: $R(t) \propto t^m$.

The expansion law significantly varies in different SN types. It depends on the mass and energy of the ejecta and on the matter distribution in the surrounding medium. The matter distribution is determined by the SN progenitor and properties of the companion star (if in a binary system or in a compact star cluster). The expansion law at the initial stage (determined by the ejecta mass) is close to the ballistic one, until the mass of the material swept up becomes comparable to that of the ejecta. Radio observations of SN 2012ap suggested that $m = 0.74 \pm 0.08$ during the first month of the expansion. The model of expansion of a relativistic shock [49] enables estimating the mass-loss rate of the progenitor star as $\dot{M} \sim 6 \times 10^{-6} M_\odot$ yr^{-1} [48]. For the nonrelativistic shock, we obtain $\dot{M} \sim 6 \times 10^{-5} M_\odot$ yr^{-1} [48]. This interval of mass-loss rates is typical of Wolf–Rayet stars.

Detailed observations of the light curve of SN 2009bb, in addition to the energy and expansion velocity of the relativistic ejecta, allowed estimating the evolution of the magnetic field behind the shock front using the synchrotron self-absorption model [50]. The magnetic field was found to decrease from 570 ± 48 mG at the shock radius $R = (3.4 \pm 0.3) \times 10^{17}$ cm to 43 ± 3 mG at the shock radius $R = (3.4 \pm 0.3) \times 10^{18}$ cm, which is consistent with the law $B \propto R^{-1}$. It should be borne in mind that the field estimate in [50] was obtained by assuming the energy equipartition between the emitting electrons and the magnetic field, which could have a substantial turbulent component. A magnetic field strength of the order of 0.5 G at a distance of 3×10^{17} cm from the star, obtained in [50], can result from stellar wind field compression at the shock front. This estimate assumes the presence of 1 kG and stronger fields on the progenitor star producing the stellar wind. Another possible scenario is related to the amplification of fluctuating magnetic fields due to the conversion of the shock energy into anisotropic distributions of accelerated relativistic particles that subsequently enhance turbulent magnetic fields (see Section 6.1). Both mechanisms encounter difficulties in attempting to reproduce high magnetic fields in SN 2009bb estimated in [50].

The plasma number density in a fast spherically symmetric wind from a Wolf–Rayet star with a constant mass-loss rate $\dot{M}$ at the distance R_{17} (in units of 10^{17} cm) is $n \approx 2\dot{M}_{-5}\, R_{17}^{-2}\, V_{\rm w8}^{-1}$ [cm^{-3}]. Here, the wind velocity $V_{\rm w8}$ is in units of 10^3 km s^{-1}. In such a wind, the kinetic energy density in a mildly relativistic shock at the distance R_{17} enables magnetic field amplification up to values slightly above 0.1 G by assuming the effective shock kinetic energy conversion into the energy of the fluctuating magnetic field with $\varepsilon_B \sim 0.1$, which is consistent with the conclusion in [43]. We note that realistic models should take the anisotropic character of stellar winds into account, with the possible formation of equatorial disks.

In Section 5, some possible magnetic field amplification and particle acceleration mechanisms by both nonrelativistic and relativistic shock waves are considered.

5. Particle acceleration and magnetic field amplification in supernova shocks

An important feature of collisionless shocks in cosmic plasma is the possibility of forming nonthermal particle distributions near the shock fronts, which can extend to relativistic energies in the case of SNe. The first studies of the structure of collisionless shocks in plasma by R Z Sagdeev carried out more than 50 years ago suggested an important role of reflection of particles from strong nonlinear magnetic field fluctuations responsible for the collisionless dissipation mechanism in fast shocks [51, 52]. Strong nonlinearity and the importance of stochasticity in dissipative processes greatly restrict the applicability of analytic models. The most detailed description of the microscopic structure of shocks can be obtained using direct numerical plasma modeling, in particular, by particle-in-cell (PIC) methods. This model is the most effective for describing relativistic shocks [53–55]. On the other hand, the very broad dynamical range of turbulent fluctuation scales and extended hard energy spectra of accelerated particles in nonrelativistic shocks require the development of approximate approaches, such as hybrid modeling [56] and Monte Carlo simulations [57, 58].

Models of collisionless shocks in supernovae. Three-dimensional PIC simulations of nonrelativistic shocks in an electron–ion plasma with the full treatment of electrons and ions and with a realistic mass ratio $m_{\rm p}/m_{\rm e}$ require very large (and frequently unrealistic) computational resources. In supersonic baryonic flows, ions mainly contribute to the momentum–energy flux in front of the shock, and therefore modeling the shock structure can be performed using a hybrid PIC approach [52, 59, 60]. The hybrid simulations consider the full dynamics of ions in self-consistent fields, with electrons treated as a massless fluid. The self-consistent electromagnetic fields in the hybrid model are calculated in the approximation of the electron neutralizing fluid, ignoring the displacement currents. Therefore, this method is mainly applicable to nonrelativistic flows, and its application to relativistic flows requires special conditions. The hybrid models allow calculating the shock structure on spatial scales exceeding $10^4\, l_{\rm i}$, where

$$l_{\rm i} = \sqrt{\frac{m_{\rm p} c^2}{4\pi n_{\rm i} e^2}} \approx 2 \times 10^7 n_{\rm i}^{-1/2} \ [\text{cm}] \tag{4}$$

is the ion inertial length. Here, the electron $n_{\rm e}$ and ion $n_{\rm i}$ number densities are expressed in cm^{-3}.

The algorithm of the hybrid PIC method for shock modeling reduces to solving the system of equations [59, 60]

$$\frac{\mathrm{d}\mathbf{r}_k}{\mathrm{d}t} = \mathbf{V}_k \,,$$

$$\frac{\mathrm{d}\mathbf{V}_k}{\mathrm{d}t} = \frac{Z_k}{m_k} \left(\mathbf{E} + \mathbf{V}_k \times \mathbf{B}\right), \tag{5}$$

$$\nabla \times \mathbf{B} = \mathbf{J} \,, \tag{6}$$

$$\frac{\partial \mathbf{B}}{\partial t} = -\nabla \times \mathbf{E} \,, \tag{7}$$

$$\mathbf{E} = \frac{1}{n} (\nabla \times \mathbf{B}) \times \mathbf{B} - \frac{1}{n} (\mathbf{J} \times \mathbf{B}) \,, \tag{8}$$

where $\mathbf{r}_k$, V_k, Z_k, m_k are the coordinates, velocities, charge, and mass of the kth ions, $\mathbf{E}$ and $\mathbf{B}$ are the electric and magnetic fields, and n and $\mathbf{J}$ are the charge density and current of ions. Equation (8) can be conveniently rewritten in the form

$$E_k = -\frac{1}{n} \frac{\partial P^B_{jk}}{\partial x_j} - \frac{1}{n} (\mathbf{J} \times \mathbf{B})_k \,, \tag{9}$$

where $P^B_{jk} = (B^2/2)\, \delta_{jk} - B_j B_k$ is the magnetic pressure tensor.

Here and below, all variables are normalized to the inertial length $l_{\rm i}$, the gyrofrequency $\Omega_{\rm i}$, the mass M_0, and the charge of ions Z_0 with the smallest space and time scales, as well as to the mean magnetic field B_0 and the unperturbed plasma density ρ_0. This normalization allows applying the results to plasmas of various compositions by space–time rescaling. The charge states of ions are assumed to be constant at distances of the order of the collisionless shock front width, i.e., of the order of several dozen ion inertial lengths $l_{\rm i}$, which is apparently the case in plasmas with the number density less than 10^{14} cm^{-3}.

In the hybrid PIC equations (4)–(8), electromagnetic fields and positions of ions are mutually dependent, which renders the problem self-consistent. Such problems can be conveniently solved numerically using the well-known leapfrog method, which has the second-order precision in time. In this method, the positions and velocities of particles are known at a step n, and electromagnetic fields are calculated at the step $n + 1/2$.

The modeling requires the shock to be initialized, which is done by the method of reflection of a supersonic particle flow from an immobile conducting wall located at $x = 0$. As a result, a shock front is formed moving in the positive x direction. A constant injection of the supersonic flux of particles with a Maxwellian distribution is performed at the opposite end of the model space, where an open boundary is set. Thermal velocities of the injected particles of different species are usually taken to be the same, i.e., the temperature ratio of ions is equal to their mass ratio. Periodic boundary conditions are set along the y and z coordinates.

Calculations using different versions of the method in [52] showed that in collisionless shocks, the width of the magnetic field profile in quasi-transverse shocks is much smaller than $\sim 10 l_{\rm i}$, while in quasi-longitudinal shocks, the shock fronts are much wider, with the characteristic width $\gtrsim 100 l_{\rm i}$. Figures 2–4 [59, 60] show the results of a three-dimensional hybrid modeling of a collisional shock structure with different magnetic field inclination angles to the shock front normal. A quasi-longitudinal shock with the Alfvén Mach number 10.0 propagating in the electron–proton plasma with a small admixture of oxygen OII ions has inclination angles to the external magnetic field $\theta = 10°$ (Fig. 2) and $\theta \approx 90°$ (Fig. 4).

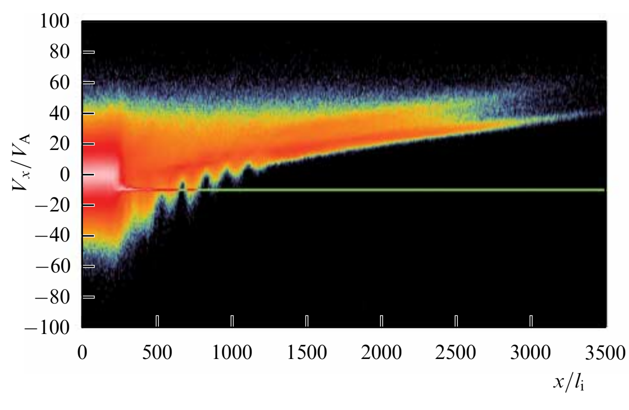

Figure 2. (Color online.) Phase space (x, V_x) of hydrogen ions in a quasi-parallel shock wave with the Alfvénic Mach number 10.0, the thermal-to-magnetic pressure ratio $\beta = 0.002$, and the magnetic field inclination to the shock front $\theta = 10°$ [60].

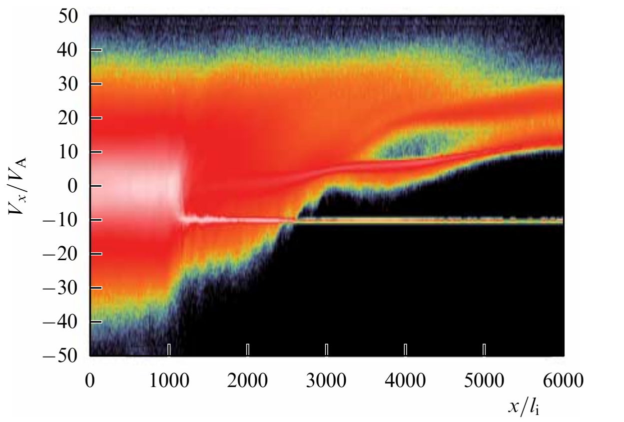

Figure 3. (Color online.) Phase space (x, V_x) of O II ions in a quasi-parallel shock wave with the Alfvénic Mach number 10.0, the thermal-to-magnetic pressure ratio $\beta = 0.002$, and the magnetic field inclination to the shock front $\theta = 10°$ [60].

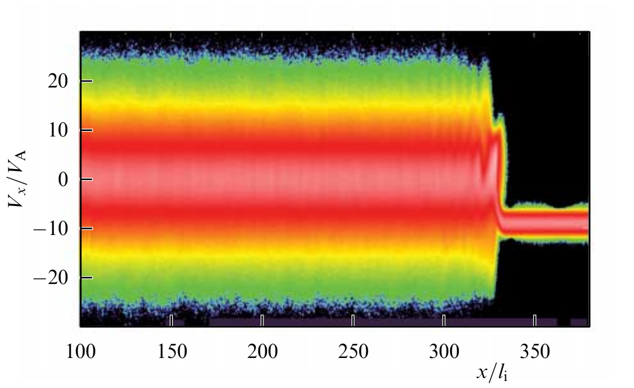

Figure 4. (Color online.) Phase space (x, V_x) of hydrogen ions in a perpendicular shock wave with the Alfvénic Mach number 9.0, the thermal-to-magnetic pressure ratio $\beta = 2.0$, and the magnetic field inclination to the shock front $\theta = 90°$ [60].

The calculations were performed for an initially cold plasma with a low thermal-to-magnetic pressure ratio $\beta \sim 0.02$. The shock propagates along the x axis. The figures show the projection of the phase space of particles (x, V_x). The reflecting wall is on the left, and cold supersonic and super-Alfvénic ion flows are injected from the right. Figures 2 and 4 show the phase space of protons for different shock inclination angles, and Fig. 3 for single-ionized oxygen ions in a longitudinal shock.

The modeling of collisionless shocks in a multi-component plasma with different magnetic field inclination angles to the shock front normal clearly showed the emergence of a distinctive precursor, the region before the shock front excited by the reflected and accelerated particles. Figure 3 suggests that before the front of a shock with a small inclination angle θ, there is a significant population of energetic heavy particles of admixed oxygen ions. For the dominating hydrogen ions, the precursor effect is also seen in Fig. 2, but is less pronounced. At the same time, the population of energetic ions in the case of the quasi-transverse shock in Fig. 4 is not seen. The transverse velocities of the reflected particles of both sorts exhibit almost harmonic quasi-periodic perturbations in the precursor. Because of the absence of Coulomb relaxation, the supra-thermal particles in the precursor, are injected into a Fermi acceleration cycle. The energy amplification in the Fermi acceleration mechanism is due to multiple crossing of the shock front by fast supra-thermal particles involved in the acceleration process [61–64]. Fermi-accelerated high-energy ions and electrons produce a nonthermal radiation in SN remnants observed from radio to gamma-ray ranges. They are also cosmic-ray sources.

6. Modeling of supernova shocks with efficient particle acceleration

In a collisionless plasma, a nonequilibrium distribution of particles perturbed by a field variation does not relax to the Maxwellian one at the characteristic time scales of the process. The slowness of the Coulomb relaxation leads to the formation of a strongly nonequilibrium distribution with particle injection into the effective Fermi acceleration region. In extended SN shocks, this forms particle spectra exhibiting both quasi-thermal peaks and power-law tails extending to an energy exceeding the thermal peaks by many orders of magnitude. Moreover, angular distributions of the accelerated particles have a noticeable anisotropy. Instabilities of a plasma with anisotropic relativistic components lead to the effective amplification of magnetic fluctuations both with resonance wavelengths (close to the gyroradius of the accelerated particles) and with nonresonance ones (short-wavelength and long-wavelength) [65–69].

Thus, extended spectra of magnetic fluctuations are formed with amplitudes exceeding that of the quasi-homogeneous initial field. As a result, a significant fraction of the kinetic energy density of the incident flow can be transformed into high-energy particle pressure. In turn, high-energy particles penetrate far into the incident plasma flow. Ponderomotive forces caused by the pressure gradient of accelerated particles slow down the incident plasma flow before the front, and instabilities related to the anisotropy of supra-thermal particles can effectively amplify fluctuating magnetic fields in the shock precursor. The effect of deceleration of the initially cold super-Alfvénic flow incident on the shock front in the

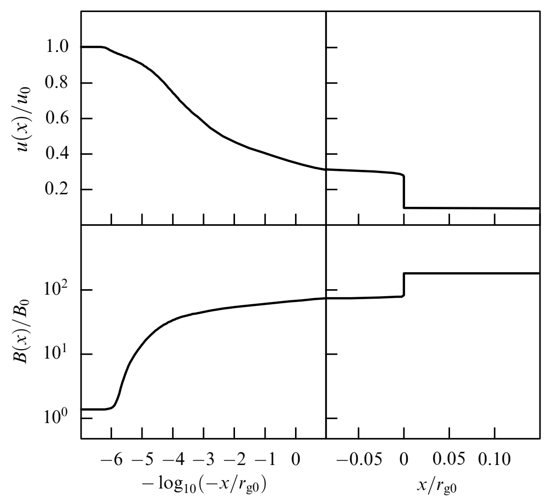

Figure 5. Macroscopic plasma velocity profiles $u(x)$ and the magnetic field B in the precursor and behind a strong quasi-longitudinal shock wave moving at the velocity of 5000 km s^{-1} and modified by the pressure of Fermi-accelerated relativistic particles. The calculations are performed by a nonlinear Monte Carlo method [57]. The microscopic structure of the viscous jump of the velocity at $x = 0$ should include the fine structure corresponding to the phase density variations shown in Fig. 2. However, the Monte Carlo calculations cannot resolve this fine structure.

precursor before the viscous jump is illustrated in Fig. 5. The extended precursor is formed due to the acceleration of particles escaping into the region before the front, where the magnetic field is effectively amplified.

An accurate modeling of the structure of a collisionless shock with the acceleration of nonthermal particles taken into account requires the use of a self-consistent description (not restricted by perturbation theory approximations) of the multi-component system with a wide range of scales of the relevant physical processes, including strong MHD turbulence and its dynamics. Indeed, microscopic PIC modeling requires the resolution of scales $L_{\rm cell} < c/\omega_{\rm pe}$ that are shorter than the electron scales $l_{\rm e} = c/\omega_{\rm pe}$, where $\omega_{\rm pe} = (4\pi n_{\rm e} e^2/m_{\rm e})^{1/2}$. The time step of the calculation $t_{\rm tstep}$ should satisfy the condition $t_{\rm tstep}\omega_{\rm pe} < 1$. The modeling of a flow with a shock modified by nonthermal particles with a hard energy spectrum extending to $E_{\max}$ should be performed in a region no smaller in size than the penetration depth of energetic particles into the shock pre-front, $L_{\rm CR} = D(E_{\max})/v_{\rm sh}$, where $D(E)$ is the diffusion coefficient of the energetic acceleration particles. A minimal estimate of $L_{\rm CR}$ assumes that the particle scattering mean free path should not be smaller than the gyroradius $r_{\rm g}$, whence $L_{\rm CR} \gtrsim r_{\rm g}(E_{\max})\, c/(3v_{\rm sh})$. Thus, the number of space cells needed for a full PIC microscopic modeling with the parameter $f = m_{\rm p}/m_{\rm e}$ is

$$\frac{D(E_{\max})/v_{\rm sh}}{c/\omega_{\rm pe}} \sim 6\times 10^{11}\left(\frac{E_{\max}}{1\,{\rm TeV}}\right)\left(\frac{v_{\rm sh}}{1000\,{\rm km\ s^{-1}}}\right)^{-1} \times\left(\frac{B}{1\ \mu{\rm G}}\right)^{-1}\left(\frac{n_{\rm e}}{\rm cm^{-3}}\right)^{1/2}\left(\frac{f}{1836}\right)^{1/2}. \qquad (10)$$

The characteristic time of the Fermi acceleration of particles by the shock is $\tau_{\rm acc}(E_{\max}) \propto D(E_{\max})/v_{\rm sh}^2$. The number of time steps needed to accelerate a particle to the energy $E_{\max}$ is

$$\tau_{\rm acc}(E_{\max})\,\omega_{\rm pe} \sim 6\times 10^{14}\left(\frac{E_{\max}}{1\,{\rm TeV}}\right)\left(\frac{v_{\rm sh}}{1000\,{\rm km\ s^{-1}}}\right)^{-2} \times\left(\frac{B}{1\mu{\rm G}}\right)^{-1}\left(\frac{n_{\rm e}}{\rm cm^{-3}}\right)^{1/2}\left(\frac{f}{1836}\right)^{1/2}. \qquad (11)$$

For nonrelativistic shocks in SN remnants, the computational resources are highly demanding, even for artificially diminished f. The use of the hybrid PIC model with a description of electrons as a fluid and a spatial resolution of the order of the gyroradius of an ion with the energy $E_{\rm th}$ somewhat relaxes these requirements, but still, they can hardly be achieved at present in three-dimensional calculations:

$$\frac{D(E_{\max})/v_{\rm sh}}{r_{\rm g0}} \sim 7\times 10^{7}\left(\frac{E_{\max}}{1\,{\rm TeV}}\right) \times\left(\frac{v_{\rm sh}}{1000\,{\rm km\ s^{-1}}}\right)^{-1}\left(\frac{E_{\rm th}}{1\,{\rm keV}}\right)^{-1/2}. \qquad (12)$$

In the hybrid model, it is also difficult to include the inverse electron current, which plays a significant role in the important Bell instability [66, 68].

Because of the need to perform calculations in a very broad dynamical range of scales of particle fluctuations and energies, direct PIC methods do not presently allow the shock modification by nonthermal particles (i.e., the 'macroscopic' structure of such flows) to be fully taken into account. Nevertheless, the role of these methods is very important for understanding micro processes in cosmic plasma.

Presently, there are several approaches to a simplified description of a multi-component strong shock structure using different methods of parameterization of the transport mechanism of high-energy particles in the extended shock precursor and of the structure of a viscous jump in the interstellar plasma. The use of the convection–diffusion transfer equation enables modeling the spectra of particles accelerated during the propagation of a spherical shock in SN remnants [70–75]. The diffusion models allow obtaining nonstationary spectra of accelerated particles with a realistic description of the SN shell. Such models assume a parameterization of the particle injection law and a simplified description of nonlinear amplification mechanisms of magnetic fields. Nonlinear Monte Carlo simulations are typically performed for stationary plane quasi-parallel shocks. However, they do not require a parameterization of the injection velocity, enable a more systematic description of nonlinear effects, and are not restricted by the assumption of the diffusion transfer of particles (for example, allow superdiffusion transfer regimes in the turbulence region [58]). Therefore, the choice of which particular model to use depends on the specifics of the problem.

Earlier, it was noticed that the interpretation of radio SN observations suggests a very high magnetic field energy density behind the shock front. Observations of galactic SN remnants suggest an effective particle acceleration to energies above 10 TeV. In what follows, to illustrate the possibility of the amplification of fluctuating magnetic fields and particle acceleration to high energies, we briefly present the results of a nonlinear macroscopic Monte Carlo modeling of collisionless quasi-longitudinal shocks in a strongly nonequilibrium turbulent plasma with relativistic components [57, 58, 76–78]. But first, we discuss the amplification mechanism of magnetic fluctuations, which plays an important role in the modeling of nonthermal processes in SN shocks.

6.1 Superadiabatic amplification of a magnetic field by shocks

The free energy of inhomogeneous anisotropic distributions of relativistic particles accelerated in the extended precursor of a strong nonrelativistic shock is the source of a significant nonadiabatic amplification of magnetic field fluctuations with a certain wavelength. Relativistic particles can contain a significant fraction of the kinetic energy of the incident nonrelativistic plasma flow. The interaction of relativistic accelerated protons with the incident plasma flow can be described following [66] by the equation of motion of the background plasma

$$\rho\left(\frac{\partial\mathbf{u}}{\partial t} + (\mathbf{u}\nabla)\,\mathbf{u}\right) = -\nabla P + \frac{1}{c}(\mathbf{j}\times\mathbf{B}) + e(n_{\rm i} - n_{\rm e})\,\mathbf{E} + \nu\triangle\mathbf{u}\,, \qquad (13)$$

where $\mathbf{u}$ and $\mathbf{j}$ are the macroscopic velocity and electric current of the background plasma. The viscosity ν is due to both collisions and collective plasma processes. Because the Debye radius of the ensemble of accelerated relativistic particles exceeds the typical size of the problem, the quasi-neutrality condition $n_{\rm i} + n^{\rm cr} = n_{\rm e}$ relates the electron and proton number densities $n_{\rm e}$ and $n_{\rm i}$ in a background plasma with a low admixture of the energy-containing relativistic component $n^{\rm cr}$. Electric currents of both the background $\mathbf{j}$ and relativistic $\mathbf{J}^{\mathrm{cr}}$ plasmas generate a magnetic field in an ideally conducting medium. In a slow MHD flow, the displacement current can be disregarded:

$$\operatorname{rot}\mathbf{B} = \frac{4\pi}{c}\,(\mathbf{j} + \mathbf{J}^{\mathrm{cr}})\,, \quad \mathbf{E} = -\frac{1}{c}\,(\mathbf{u}\times\mathbf{B})\,. \tag{14}$$

The induction equation then takes the form

$$\frac{\partial\mathbf{B}}{\partial t} = \nabla\times(\mathbf{u}\times\mathbf{B}) + \nu_{\mathrm{m}}\triangle\mathbf{B}\,, \tag{15}$$

where ν_{m} is the magnetic viscosity. If the unperturbed magnetic field was homogeneous, the current compensation condition must be satisfied in Eqn (14).

Thus, equation of motion (13) reduces to the form

$$\rho\left(\frac{\partial\mathbf{u}}{\partial t} + (\mathbf{u}\nabla)\,\mathbf{u}\right) = -\nabla P + \frac{1}{4\pi}\,(\nabla\times\mathbf{B})\times\mathbf{B} - \frac{1}{c}\,(\mathbf{J}^{\mathrm{cr}} - en^{\mathrm{cr}}\mathbf{u})\times\mathbf{B} + \nu\triangle\mathbf{u}\,. \tag{16}$$

The relativistic particle current $\mathbf{J}^{\mathrm{cr}}$ induces an inverse current in the background plasma [66]. By treating the relativistic current in Eqn (16) as an external one, Bell carried out the linear stability analysis of the system with small perturbations $\propto \exp(\gamma t + \mathrm{i}\mathbf{kr})$, where γ is the instability growth rate. Bell discovered that in a certain region of parameters, the ponderomotive force acting on the plasma is dominated by the term with the external current $\mathbf{J}^{\mathrm{cr}}\times\mathbf{B}/c$. This condition holds for magnetic field fluctuations with $k < k_1$, where

$$k_1 = \frac{4\pi}{c}\,\frac{J_0^{\mathrm{cr}}}{B_0}\,. \tag{17}$$

In systems with a strong relativistic particle current $\mathbf{J}^{\mathrm{cr}}$, short-wavelength fluctuations with wavelengths smaller than the gyroradius of relativistic protons, $r_{\mathrm{g0}}k > 1$, rapidly grow.

In a cold background plasma with the sound velocity much lower than the Alfvén velocity V_{A} (which is usually the case in SN shocks), the linear growth rate of the Bell instability in the wavelength range $r_{\mathrm{g0}}^{-1} < k < k_1$ can be represented in the form

$$\gamma \approx \gamma_{\max}\,\frac{k_z}{k}\,, \tag{18}$$

where k_z is the projection of the wave vector on the unperturbed field direction and

$$\gamma_{\max} = V_{\mathrm{A}}\sqrt{k_1|k| - k^2}\,. \tag{19}$$

The cold plasma approximation in Eqn (19) can be used if

$$\left(\frac{V_{\mathrm{A}}}{v_{T\mathrm{i}}}\right)^2 > k_1 r_{\mathrm{g0}}\,\frac{V_{\mathrm{A}}}{c}\,, \tag{20}$$

where $v_{T\mathrm{i}}$ is the thermal ion velocity.

Unstable Bell modes, unlike Alfvén waves, have a growth rate much larger than the real part of the frequency. Another important feature of these modes is that their kinetic energy density is higher than the magnetic energy density:

$$|\mathbf{v}(\mathbf{k})|^2 \approx \frac{1}{4\pi\rho}\,\frac{k_1}{|k_z|}\,|\mathbf{b}(\mathbf{k})|^2\,, \tag{21}$$

where $k_1 > k_z$.

If the current is represented as $J_0^{\mathrm{cr}} \approx |\varDelta_{1,0}|\,en_{\mathrm{cr}}c$, where $|\varDelta_{1,0}|$ is the measure of anisotropy of relativistic protons, the instability condition can be expressed as

$$|\varDelta_{1,0}| > \frac{B^2}{4\pi E_{\mathrm{cr}}}\,, \tag{22}$$

where E_{cr} is the energy density of relativistic accelerated particles.

For long-wavelength fluctuations with $r_{\mathrm{g0}}k < 1$, the Bell instability is absent. This is related to the relativistic particle current $\mathbf{J}^{\mathrm{cr}}$ being highly sensitive to magnetic field fluctuations imposed on the system [79]. For long-wavelength fluctuations, $\mathbf{J}^{\mathrm{cr}}$ is no longer a constant and externally given current. For these wavelengths, other instabilities, slower than the short-wavelength Bell one, arise. On the other hand, long-wavelength fluctuations with $r_{\mathrm{g0}}k \lesssim 1$ effectively scatter the most energetic particles in the accelerator and are therefore important for the formation of spectra of protons and nuclei [69, 79].

6.2 Maximum energy of ions accelerated in magnetohydrodynamic flows

In many cases, particle acceleration to relativistic energies occurs during the interaction with highly conducting MHD plasma flows, which can be characterized by the Lorentz factor Γ_{flow} and the dimensionless flow velocity β_{flow}. Electric fields in MHD flows are induced by the plasma motion with frozen magnetic fields. Despite a rich variety of MHD flows, including shocks, flows with velocity gradients, and colliding supersonic flows, some very general estimates of the maximum available energy of accelerated particles can be obtained [80]. These estimates are based on the scarcely available particle acceleration rate in MHD flows. The scattering time of a particle τ_{s} is limited by the inverse particle gyrofrequency: $\tau_{\mathrm{s}} \sim \eta\omega_B^{-1}$, where $\eta \geqslant 1$. The particle acceleration time for Fermi acceleration is $\tau_{\mathrm{a}} \sim \beta_{\mathrm{flow}}^{-2}\,\tau_{\mathrm{s}}$. The maximum energy of the accelerated particle can be estimated from the condition that the time $\tau_{\mathrm{a}}(E)$ is shorter than the dynamical time of particle retention in the comoving frame. For a particle with a charge Z interacting with an MHD flow, it is possible to estimate the magnetic luminosity $\mathcal{L}_{\mathcal{M}}$ determined by the electromagnetic energy flux generated by an energy source with the collimation angle θ_{m}:

$$\mathcal{L}_{\mathcal{M}} > 6\times10^{44}\,\theta_{\mathrm{m}}^2\beta_{\mathrm{flow}}^{-1}\Gamma_{\mathrm{flow}}^2\eta^2 Z^{-2}E_{20}^2\ [\mathrm{erg\ s^{-1}}]\,, \tag{23}$$

where E_{20} is the energy of the accelerated particle in units 10^{20} eV. We note that according to [80], in the limit $\theta_{\mathrm{m}}\to 0$, we have

$$\mathcal{L}_{\mathcal{M}} \sim 10^{45}\,\eta^2\beta_{\mathrm{flow}}^{-3}Z^{-2}E_{20}^2\ [\mathrm{erg\ s^{-1}}]\,.$$

Estimate (23) is valid for ions in relatively rarefied flows, because the particle energy losses were ignored in its derivation. The magnetic field freezing condition used when deriving formula (23) is violated in current sheets formed during the magnetic reconnection process. Particle acceleration during magnetic reconnection is efficient in systems with a dominating magnetic field energy density [81, 82].

PIC simulations of the particle acceleration by relativistic shocks [54] demonstrated that in this case, $E_{\max}\propto t^{1/2}$, i.e., the acceleration occurs significantly more slowly than expected in the Bohm diffusion regime corresponding to

$\eta \sim 1$. This result is related to the dominance in relativistic shocks with $\Gamma_{\text{flow}} \gg 1$ of short-wavelength Weibel fluctuations, on which the scattering occurs much more slowly than in the Bohmian regime.

In the case of particle acceleration in SN shocks, Eqn (23) suggests that mildly relativistic shocks in SNe with $\beta_{\text{flow}}\Gamma_{\text{flow}} \sim 1$ are optimal to attain the maximum energy for a given power of the source $\mathcal{L}_{\mathcal{M}}$. These flows are realized in relativistic SNe and in pulsar-wind nebulae with bow shocks [83]. Below, we present some results of Monte Carlo modeling of the particle acceleration in these objects.

6.3 Particle acceleration and magnetic field amplification by nonrelativistic shocks

The strong nonlinear relation among particle injection, the shock structure, and the magnetic field amplification makes the Monte Carlo method especially useful. This method enables an iterative calculation of the shock velocity and the particle distribution function consistent with the conservation of mass, momentum, and energy and takes a nonlinear feedback from accelerated high-energy particles into account. Figure 6 shows the results of calculations of the macroscopic structure of an extended front of a strong shock propagating with a velocity v_{sh} in a turbulent plasma with the number density n_0 in the magnetic field $B_0 = 3$ μG for different values of v_{sh} and n_0 shown in the figure. The distance is measured in units $r_{\text{g}0} = m_{\text{p}}\, v_{\text{sh}}\, c/(eB_0)$ [57]. The calculations were performed in the rest frame of the viscous jump for a one-dimensional flow (particle momenta are here three-dimensional). To take the finite size of the system into account, the boundary condition of the free particle escape from the surface located at the distance $10^6\, r_{\text{g}0}$ from the viscous jump was set.

Figure 7 shows the conversion efficiency of the energy density of a plasma flow incident on the front $\Phi_{\text{p}0} = 0.5\rho_0 v_{\text{sh}}^2$ into the energy density of magnetic fluctuations $P_{\text{w},2} = B^2/(8\pi)$ calculated by the Monte Carlo method. The conversion efficiency depends on the shock velocity and reaches 10% for nonrelativistic waves but can be somewhat higher ($\sim 18\%$) for subrelativistic shock velocities. The calculations were carried out for different models of the energy transfer across the spectrum of magnetic fluctuations. The results depend on the presence or absence of the Kolmogorov cascade across the spectrum. But the model ignores the energy dissipation of turbulent fluctuations. A strong dissipation of turbulence can significantly alter the particle and turbulence spectra. In particular, in this regime, we can expect softer proton spectra than shown in Fig. 7, a lower compression degree of the plasma, and a smaller modification of the flow by the escaping cosmic rays than shown in Fig. 6. The microscopic theory of dissipation of turbulent fluctuations in a strongly nonlinear regime is as yet absent, which complicates the construction of more realistic models of particle acceleration by strong shocks.

In Fig. 6, the maximum energies of protons accelerated by nonrelativistic shocks in SN remnants are $\lesssim 100$ TeV. An analysis of the spectra and anisotropy of galactic cosmic rays suggests the probable contribution from galactic cosmic-ray sources with energies in excess of 1 PeV. These could be SNe exploding in compact clusters of massive stars forming a supersonic wind. The collision of a SN shock with the cluster wind is illustrated in Fig. 8. The particle acceleration in colliding supersonic flows allows significantly increasing the maximum available energies of the accelerated particles [84, 85].

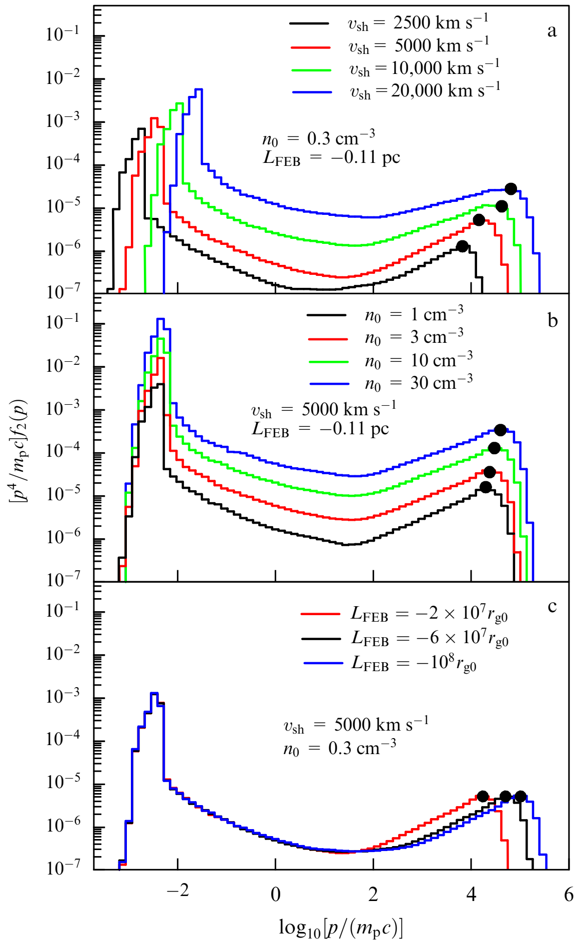

Figure 6. (Color online.) Spectra and maximum energies of accelerated particles for different (a) shock velocities v_{sh}, (b) plasma densities n_0, and (c) location of the free-escape boundary L_{FEB} [57]. Shown is a model distribution function in the phase space (multiplied by p^4) for protons accelerated by nonrelativistic shocks. The proton distribution function is calculated in the shock rest frame. The particle spectra exhibit a quasi-thermal peak and extended piece-wise power-law distributions. The spectra were calculated using a nonlinear Monte Carlo model that takes into account the amplification of the fluctuating magnetic field by instabilities of the anisotropic fast particle distribution in the precursor and a nonlinear modification of the plasma velocity profile. The black dots show the maximum values of the accelerated proton distributions f_2.

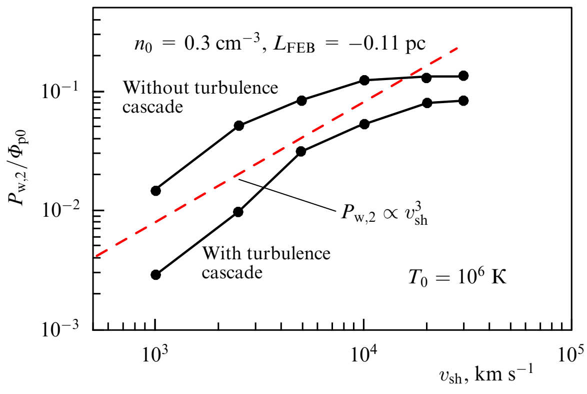

Figure 7. Model conversion efficiency ε_B of the energy of an incident plasma flow on the shock front (energy density $\Phi_{\text{p}0}$) into magnetic fluctuations with the energy density $P_{\text{w},2}$ behind the shock front as a function of the shock velocity v_{sh} [57].

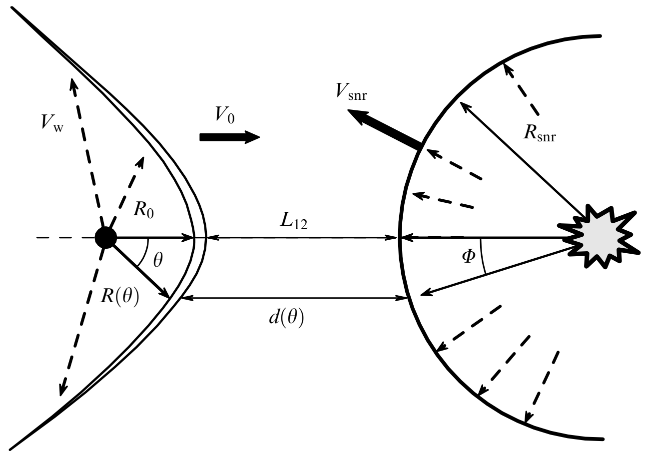

Figure 8. Geometry of the collision of a supernova shock (right source) with the supersonic wind from a compact massive star cluster [84, 85].

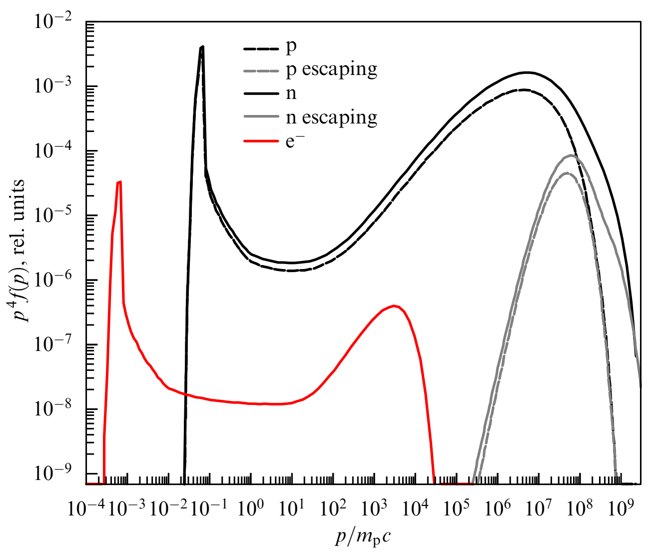

Figure 9. (Color online.) Model cosmic-ray spectra from a supernova shell colliding with the intense wind from the compact young massive star cluster shown in Fig. 8 [84, 85].

Figure 9 shows the model spectra of protons (p), different kinds of nuclei (n), and electrons (e^-) (red curve) accelerated in the collision region of as SN shell with an intense stellar wind from a young star cluster. The upper black curves show the spectrum of nuclei in the source, and the lower relatively narrow curves show the spectra of particles escaping from the source. A feature of this model is the presence of a hard spectral tail for particle energies above 10 GeV.

Figure 10 shows the gamma-ray (dashed and dotted curves) and neutrino (solid curve) spectra formed by accelerated particles in the collision region of a SN remnant with an intensive stellar wind from a young star cluster for the young galactic star cluster Westerlund I (WdI). The emission spectra are shown for the moment 400 years after the SN explosion in the WdI cluster [84, 85]. Neutrinos and most of the gamma quanta are produced by inelastic collisions of the accelerated protons with the surrounding medium (contribution to the gamma-ray emission due to Compton scattering of the accelerated electrons is shown by the dashed curve). Shown also are the gamma-ray fluxes observed by the

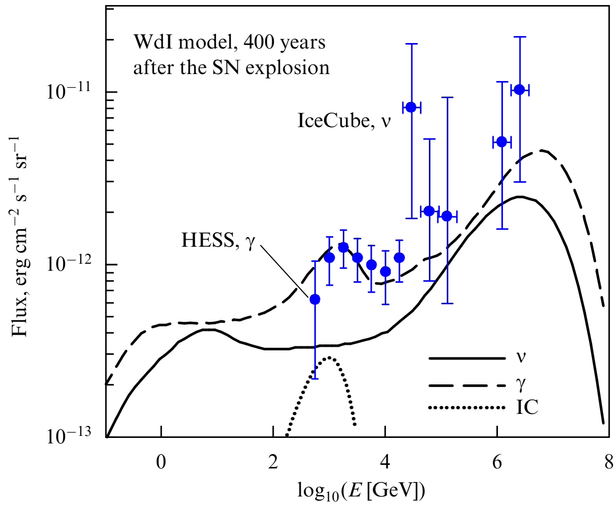

Figure 10. Gamma-ray (γ) and high-energy neutrino (ν) spectra calculated using the model of a SN colliding with the wind from a young massive star cluster. Such sources can explain some high-energy neutrino events observed by the IceCube (IC) neutrino observatory [85].

ground-based Cherenkov imaging telescope HESS (High-Energy Stereoscopic System) and estimates of the high-energy neutrino fluxes detected by the IceCube neutrino observatory (from the vicinity of the WdI cluster).

6.4 Particle acceleration and magnetic field amplification in relativistic supernovae

Radio observations of SN 2009bb discussed in Section 4 [44] suggest that SN shocks can have mildly relativistic velocities with $\beta\Gamma \sim 1$ for several months after the SN explosion. Based on the discussion in Section 6.2, such objects can be expected to accelerate particles to energies above 1 PeV. The results of calculations of proton spectra in a nonlinear Monte Carlo model with the magnetic turbulence amplification by instabilities of anisotropic distributions of accelerated particles taken into account are presented in Fig. 11 (the particle spectrum in the shock is shown in its rest frame) and in Fig. 12 (the spectrum of escaping particles is shown in the frame of a remote observer). The calculations assumed that the magnetic field in the wind of a Wolf–Rayet star — the SN progenitor — has equal regular and random components with a total amplitude of 0.01 G at a distance of 10^{17} cm from the star. The turbulent magnetic field behind the shock front with $\Gamma \sim 1.5$ is about 0.2 G.

7. Gamma-ray bursts and type-Ic relativistic supernovae

Existing models of gamma-ray bursts assume the presence of a strongly collimated relativistic outflow with a Lorentz factor of the order of 100, in which fast and efficient conversion of the kinetic or magnetic energy into the observed gamma-ray radiation occurs [87–89]. Figure 1 shows possible distributions of the ejecta energy over four-velocities that distinguish possible emission sources emerging after a massive star collapse. Gamma-ray bursts shown in purple have a very flat energy distribution. Relativistic SNe powered by a prolonged energy release from the central compact source demonstrate an energy distribution intermediate between gamma-ray bursts and ordinary type-Ic SNe. Long, rela-

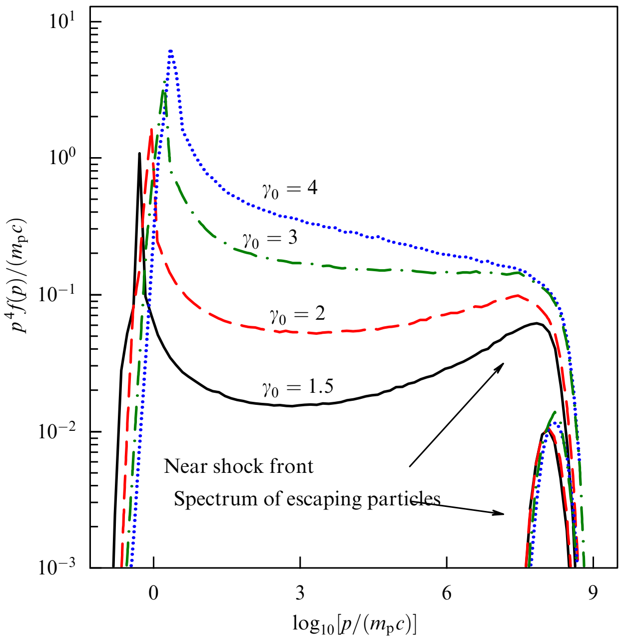

Figure 11. Proton spectra in the shock rest frame calculated in a nonlinear model with the feedback from the accelerated particles on the shock front structure taken into account. Shown are the distribution functions in the phase space (multiplied by p^4) for Fermi-accelerated protons calculated in the shock rest frame. The particle spectrum clearly exhibits a quasi-thermal peak and extended piecewise power-law segments. The spectra are calculated using a nonlinear Monte Carlo model (see [57, 86]). The model includes the amplification of the fluctuating magnetic field by instabilities of the anisotropic fast particle distribution in the precursor and a nonlinear modification of the plasma velocity profile. Different curves correspond to different values of the four-velocity of a plane shock.

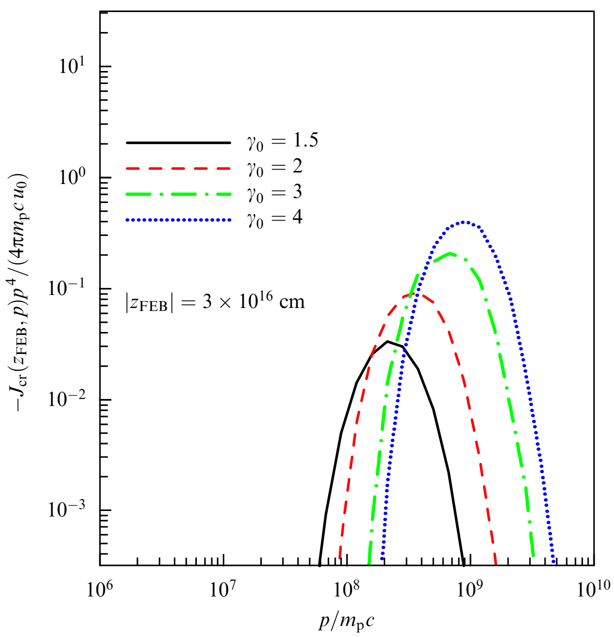

Figure 12. Distribution functions in the phase space (multiplied by p^4) for protons escaping the acceleration region of particles by the shock. The proton distribution function is calculated in the rest frame of the circumstellar medium through which the shock propagates. $z_{\rm FEB}$ is the location of the boundary of free-escaping particles, $J_{\rm cr}(z_{\rm FEB}, p)$ is the spectral flux density of the accelerated protons through the free-escape boundary.

tively soft gamma-ray bursts can be related to the core collapses of massive rotating stars, which for some stellar parameters are not accompanied by the formation of a strong shock propagating from the star center outwards, as in the case of type-Ibc SNe [90]. The accretion of matter onto a rapidly rotating black hole can likely produce collimated relativistic jets in collapsars [91, 92] with the later generation of a gamma-ray burst. A stellar collapse in which the relativistic jet from the central source does not pierce the stellar envelope can be a source of high-energy neutrinos without the associated gamma-ray emission [93].

The population of hard gamma-ray bursts with a duration shorter than 2 s cannot be described by this model. Popular models of short gamma-ray bursts are based on the idea of coalescence of a neutron star with another neutron star or a black hole (although other scenarios of the compact star coalescence not leading to a gamma-ray burst are possible) [94–96]. The energy and angular momentum loss due to the gravitational wave emission enable the formation of a rapidly spinning black hole with a high accretion rate of matter left over after the coalescence. The accretion is accompanied by energy release due to neutrino–antineutrino annihilation or due to magneto-rotational effects of accreting black holes [92, 97]. The coalescence is accompanied by an ejection of neutron-rich matter and active r-nucleosynthesis, which produces a substantial fraction of the observed stable isotopes with an atomic number higher than 60. The relativistic outflows and hypernovae likely played a significant role in the nucleosynthesis during the epoch of the first (Population III) stars [98].

A beautiful confirmation of the above model of short gamma-ray bursts was obtained by the observation of gamma-ray emission by the Fermi and INTEGRAL (INTernational Gamma-Ray Astrophysical Laboratory) observatories [99, 100] several seconds after the detection of gravitational waves from the source GW170817 by the Advanced LIGO (Laser Interferometer Gravitational-wave Observatory) and Advanced Virgo detectors [101]. In the compact star coalescence scenario [95], as well as in the model of tidal disruption of stars by massive black holes [102], calculations predict the formation of relativistic outflows with shocks.

Modeling the prompt emission at the initial stage of a gamma-ray burst requires mechanisms for conversion of the energy released during the collapse into the observed hard gamma-ray emission. The conversion mechanisms depend on the initial magnetization of the relativistic outflow, which can be conveniently characterized by the parameter

$$\sigma = \frac{F_b}{F_p} = \frac{B^2}{4\pi\rho c^2 \Gamma} = \frac{B'^2}{4\pi\rho' c^2}\,, \tag{24}$$

where F_b is the electromagnetic energy flux, F_p is the plasma energy flux, B is the magnetic field strength, and ρ is the density of matter (which can be an electron–positron plasma with baryonic admixture) in the laboratory frame, relative to which the outflow moves with the Lorentz factor Γ. The primed values (B' and ρ') are measured in the rest frame of the outflow. The formation of spectra of accelerated particles and radiation in a magnetized plasma outflow with $\sigma > 1$ usually assumes magnetic field dissipation by reconnection mechanisms, which have been studied for a long time in modeling solar flares and flaring phenomena in magnetospheres of Earth and other planets [82, 103–105], as well as in magnetars

[106]. Magnetic reconnection processes have been studied in a relativistic plasma, in particular in [81]. Jointly with the Fermi particle acceleration, these processes can explain the spectra of gamma-ray bursts and their afterglows [88, 89].

A particular population of transient sources includes tidal disruptions of stars by massive black holes. A star with mass $M_\star$ and radius $R_\star$ that enters the region within the radius

$$R_{\rm t} = R_\star \left(\frac{\eta_{\rm t} M_{\rm BH}}{M_\star} \right)^{1/3}$$

from a massive black hole with a mass $M_{\rm BH}$ is disrupted by tidal forces. The parameter $\eta_{\rm t}$ depends on the stellar structure. The tidal disruptions of stars by supermassive black holes result in the accretion of part of the disrupted star onto the black hole, which is accompanied by a bright outburst lasting up to several years. The remaining part of the star (with a mass comparable to the captured one) is ejected with a maximum velocity of the order of 10^4 km s^{-1} [102, 107]. As shown above, such fast super-Alfvénic outflows should be able to accelerate particles to high energies and are non-thermal emission sources. Presently, these outflows are considered to be possible sources of ultra-high-energy neutrinos and cosmic rays [108–110].

The transient source Swift J164449.3 + 573451 is an interesting example of the flaring accretion onto a black hole with a mass of the order of $10^6 - 10^7 M_\odot$. Radio and X-ray observations suggest the emergence of a mildly relativistic outflow related to the accretion of matter from a star tidally disrupted by a massive black hole [111–113].

A statistical analysis of X-ray sources that demonstrated more than an order-of-magnitude decrease in flux enabled the authors of [114] to estimate the rate of stellar tidal disruption transients by massive black holes. The obtained event rate, $\sim 3 \times 10^{-5}$ events in one year per galaxy with a redshift $z < 0.18$, is in reasonable agreement with events in the nearby Universe. A new generation of high-sensitivity X-ray [115, 116] and gamma-ray [117–119] detectors will enable significant progress in understanding the physics of bright variable high-energy sources in the coming years.

8. Conclusion

A huge energy release, up to the order of magnitude of the binding energy of a star, $\sim 10^{53}$ erg, occurs in several seconds during core collapses of massive stars or compact relativistic binary coalescences with neutron stars. It is accompanied by powerful broadband electromagnetic emission, emission of gravitational waves, intensive neutrino fluxes, and cosmic-ray acceleration. The structure of plasma outflows with relativistic and nonrelativistic components, light curves, and spectra of electromagnetic radiation are determined by the character and duration of the energy release from the central source.

In particular, in addition to the shock formation, a stellar core collapse [26] can result in the appearance of a rapidly rotating central compact object — a magnetar or a black hole — which can provide an important additional energy release. The interaction of a strongly magnetized relativistic jet or wind from the central compact source with the stellar matter and circumstellar shells can be a significant factor determining the character of the observed light curve and emission spectra [120]. Later spectral observations of the supernova remnant allow determining the structure and composition of the ejecta — the matter of the stellar envelope ejected during a supernova explosion [121].

Radio, optical, and X-ray observations of afterglows from the source GW 170817/GRB 170812A over more than 250 days after a short gamma-ray burst suggested that the afterglow spectrum does not visibly change, and the flux decrease during the first 200 days is related to the geometry of the expanding outflow [122–124].

The afterglow of the source GW 170817/GRB 170812A in a broad spectral range covering almost nine decades (from 1 GHz to 10^{18} Hz) is well fitted by a single power-law spectrum with a photon index of about 1.6. The afterglow of GRB 170817A observed for about one year is apparently the synchrotron radiation of relativistic electrons and positrons. The emitting relativistic particle acceleration is apparently related to a mildly relativistic magnetized plasma outflow. While detailed calculations of the formation and evolution of such flow will be performed only in the future, the observations are consistent with the model of a structured relativistic jet observed at some angle to the jet axis [122–127].

Mildly relativistic shocks accompanying the propagation of the structured jet from GRB 170817A in a rarefied circumstellar medium can be an effective source of cosmic rays with energies above 1 PeV. If such collisions occur in the Galaxy at a rate of 10^{-5} events per year, their contribution to the observed cosmic ray spectrum can be significant, along with that due to relativistic SNe capable of accelerating cosmic rays to even higher energies of the order of 10^{18} eV [86].

An estimate of the galactic rate of binary neutron star coalescences from 5×10^{-6} to 5×10^{-4} events per year remains uncertain as yet [128]. The coalescence of the binary neutron star generated by GW 170817/GRB 170817A provides optimal conditions to form some heavy elements by rapid neutron captures (the r-process). In particular, the authors of [128] estimated, within existing uncertainties, the respective amounts of gold and europium produced by GW 170817 to be 3–13 and 1–5 Earth masses. Modeling the redistribution of the released energy between different components of the expanding plasma outflow, electromagnetic field enhancement, particle acceleration, and emission processes discussed above enable calculating the time evolution of the radiation spectra.

Thus, modern-day detailed sigh-sensitivity observations of sources in a broad electromagnetic spectral range and high-sensitivity neutrino detectors offer a unique possibility of testing the source models based on fundamental laws in extreme natural conditions.

Acknowledgments
The author acknowledges his colleagues A E Vladimirov, P E Gladilin, A M Krasil'shchikov, Yu A Kropotina, K P Levenfish, S M Osipov, A E Petrov, I N Toptygin, Yu A Uvarov, and D C Ellison for joint research in high-energy astrophysics. The study was supported by the Program P3 of the Presidium of RAS "Physics of Fundamental Interactions and Nuclear Technologies."

References

1. Goobar A, Leibundgut B *Annu. Rev. Nucl. Part. Sci.* **61** 251 (2011)
2. Filippenko A V *Annu. Rev. Astron. Astrophys.* **35** 309 (1997)
3. Gal-Yam A *Science* **337** 927 (2012)
4. Branch D, Wheeler J C *Supernova Explosions* (Berlin: Springer-Verlag, 2017)

5. Zel'dovich Ya B, Raizer Yu P *Physics of Shock Waves and High-Temperature Hydrodynamic Phenomena* Vols 1, 2 (New York: Academic Press, 1966, 1967); Translated from Russian: *Fizika Udarnykh Voln i Vysokotemperaturnykh Gidrodinamicheskikh Yavlenii* (Moscow: Nauka, 1966)
6. Fortov V E *Moshchnye Udarnye Volny* (Powerful shocks) (Moscow: Fizmatlit, 2018)
7. Shakura N I, Sunyaev R A *Astron. Astrophys.* **24** 337 (1973)
8. Berezinskii V S et al. *Astrophysics of Cosmic Rays* (Ed. V L Ginzburg) (Amsterdam: North-Holland, 1990); Translated from Russian: *Astrofizika Kosmiceskikh Luchei* (Ed. V L Ginzburg) 2nd ed. (Moscow: Nauka, 1989)
9. Grassberg E K, Imshennik V S, Nadyozhin D K *Astrophys. Space Sci.* **10** 28 (1971)
10. Imshennik V S, Nadezhin D K *Sov. Sci. Rev. E* **8** 1 (1989) Pt. 1; *Usp. Fiz. Nauk* **156** 561 (1988)
11. Blinnikov S, in *Handbook of Supernovae* (Eds A W Alsabti, P Murdin) (Berlin: Springer, 2017) p. 843
12. Chevalier R A, Fransson C, in *Handbook of Supernovae* (Eds A W Alsabti, P Murdin) (Berlin: Springer, 2017) p. 875
13. Waxman E, Katz B, in *Handbook of Supernovae* (Eds A W Alsabti, P Murdin) (Berlin: Springer, 2017) p. 967
14. Gandel'man G M, Frank-Kamenetskii D A *Sov. Phys. Dokl.* **1** 223 (1956); *Dokl. Akad. Nauk SSSR* **107** 811 (1956)
15. Kompaneets A S *Sov. Phys. Dokl.* **5** 46 (1960); *Dokl. Akad. Nauk SSSR* **109** 49 (1956)
16. Chevalier R A *Astrophys. J.* **258** 790 (1982)
17. Klimishin I A *Udarnye Volny v Obolochkakh Zvezd* (Shocks in Stellar Envelopes) (Moscow: Nauka, 1984)
18. Gnatyk B I *Sov. Astron. Lett.* **11** 331 (1985); *Pis'ma Astron Zh.* **11** 785 (1985)
19. Litvinova I Y, Nadezhin D K *Sov. Astron. Lett.* **16** 29 (1990); *Pis'ma Astron. Zh.* **16** 61 (1990)
20. Tan J C, Matzner C D, McKee C F *Astrophys. J.* **551** 946 (2001)
21. Margutti R et al. *Astrophys. J.* **797** 107 (2014)
22. Li W et al. *Mon. Not. R. Astron. Soc.* **412** 1441 (2011)
23. Woosley S, Janka T *Nature Phys.* **1** 147 (2005)
24. Ott C D et al. *Astrophys. J.* **768** 115 (2013)
25. Couch S M et al. *Astrophys. J. Lett.* **808** L21 (2015)
26. Burrows A et al. *Space Sci. Rev.* **214** 33 (2018)
27. Summa A et al. *Astrophys. J.* **852** 28 (2018)
28. Woosley S E, Bloom J S *Annu. Rev. Astron. Astrophys.* **44** 507 (2006)
29. Gehrels N, Ramirez-Ruiz E, Fox D B *Annu. Rev. Astron. Astrophys.* **47** 567 (2009)
30. Mészáros P, Gehrels N *Res. Astron. Astrophys.* **12** 1139 (2012)
31. Lazzati D et al. *Astrophys. J.* **750** 68 (2012)
32. Piran T et al., arXiv:1704.08298
33. Katz D, Sapir N, Waxman E *Proc. Int. Astron. Union* **7** (S279) 274 (2011)
34. Ud-Doula A, Owocki S P, Townsend R H D *Mon. Not. R. Astron. Soc.* **385** 97 (2008)
35. Wade G A et al. *Mon. Not. R. Astron. Soc.* **456** 2 (2016)
36. Aurière M et al. *Astron. Astrophys.* **516** L2 (2010)
37. Kervella P et al. *Astron. Astrophys.* **609** A67 (2018)
38. Walder R, Folini D, Meynet G *Space Sci. Rev.* **166** 145 (2012)
39. Ellison D C et al. *Astrophys. J.* **744** 39 (2012)
40. Weiler K W et al. *Astrophys. J.* **740** 79 (2011)
41. Björnsson C-I, Keshavarzi S T *Astrophys. J.* **841** 12 (2017)
42. Chevalier R A *Astrophys. J.* **499** 810 (1998)
43. Chevalier R A, Fransson C *Astrophys. J.* **651** 381 (2006)
44. Soderberg A M et al. *Nature* **463** 513 (2010)
45. Mazzali P A et al. *Mon. Not. R. Astron. Soc.* **458** 3455 (2016)
46. Kulkarni S R et al. *Nature* **395** 663 (1998)
47. Li Z-Y, Chevalier R A *Astrophys. J.* **526** 716 (1999)
48. Chakraborti S et al. *Astrophys. J.* **805** 187 (2015)
49. Blandford R D, McKee C F *Phys. Fluids* **19** 1130 (1976)
50. Chakraborti S et al. *Nature Commun.* **2** 175 (2011)
51. Sagdeev R Z, in *Reviews of Plasma Physics* Vol. 4 (Ed. M A Leontovich) (New York: Consultants Bureau, 1966) p. 23; Translated from Russian: *Voprosy Teorii Plasmy* Vol. 4 (Ed. M A Leontovich) (Moscow: Gosatomizdat, 1964) p. 20
52. Marcowith A et al. *Rep. Prog. Phys.* **79** 046901 (2016)
53. Spitkovsky A *Astrophys. J. Lett.* **673** L39 (2008)
54. Sironi L, Spitkovsky A, Arons J *Astrophys. J.* **771** 54 (2013)
55. Pelletier G, Bykov A, Ellison D, Lemoine M *Space Sci. Rev.* **207** 319 (2017)
56. Lipatov A S *The Hybrid Multiscale Simulation Technology: an Introduction with Application to Astrophysical and Laboratory Plasmas* (Berlin: Springer, 2002)
57. Bykov A M et al. *Astrophys. J.* **789** 137 (2014)
58. Bykov A M, Ellison D C, Osipov S M *Phys. Rev. E* **95** 033207 (2017)
59. Kropotina Yu A et al. *Tech. Phys.* **60** 231 (2015); *Zh. Tekh. Fiz.* **85** 73 (2015)
60. Kropotina Yu A et al. *Tech. Phys.* **61** 517 (2016); *Zh. Tekh. Fiz.* **86** 40 (2016)
61. Krymskii G F *Sov. Phys. Dokl.* **22** 327 (1977); *Dokl. Akad. Nauk SSSR* **234** 1306 (1977)
62. Axford W I, Leer E, Skadron G, in *15th Intern. Cosmic Ray Conf., Plovdiv, Bulgaria, August 13–26, 1977, Conf. Papers* Vol. 11 (Sofia: B'lgarska Akademiia na Naukite, 1977) p. 132
63. Bell A R *Mon. Not. R. Astron. Soc.* **182** 147 (1978)
64. Blandford R D, Ostriker J P *Astrophys. J. Lett.* **221** L29 (1978)
65. Lucek S G, Bell A R *Mon. Not. R. Astron. Soc.* **314** 65 (2000)
66. Bell A R *Mon. Not. R. Astron. Soc.* **353** 550 (2004)
67. Bykov A M, Ellison D C, Renaud M *Space Sci. Rev.* **166** 71 (2012)
68. Schure K M, Bell A R, Drury L O'C, Bykov A M *Space Sci. Rev.* **173** 491 (2012)
69. Bykov A M et al. *Space Sci. Rev.* **178** 201 (2013)
70. Berezhko E G, Yelshin V K, Ksenofontov L K *Astropart. Phys.* **2** 215 (1994)
71. Kang H, Ryu D *Astrophys. J.* **721** 886 (2010)
72. Caprioli D, Blasi P, Amato E *Astropart. Phys.* **34** 447 (2011)
73. Zirakashvili V N, Ptuskin V S *Astropart. Phys.* **39–40** 12 (2012)
74. Bykov A M, Gladilin P E, Osipov S M *Mon. Not. R. Astron. Soc.* **429** 2755 (2013)
75. Brose R, Telezhinsky I, Pohl M *Astron. Astrophys.* **593** A20 (2016)
76. Jones F C, Ellison D C *Space Sci. Rev.* **58** 259 (1991)
77. Vladimirov A E, Bykov A M, Ellison D C *Astrophys. J.* **688** 1084 (2008)
78. Ellison D C, Warren D C, Bykov A M *Astrophys. J.* **776** 46 (2013)
79. Bykov A M, Osipov S M, Ellison D C *Mon. Not. R. Astron. Soc.* **410** 39 (2011)
80. Lemoine M, Waxman E *J. Cosmol. Astropart. Phys.* **2009** (11) 009 (2009)
81. Sironi L, Spitkovsky A *Astrophys. J. Lett.* **783** L21 (2014)
82. Zelenyi L, Artemyev A *Space Sci. Rev.* **178** 441 (2013)
83. Bykov A M et al. *Space Sci. Rev.* **207** 235 (2017)
84. Bykov A M *Astron. Astrophys. Rev.* **22** 77 (2014)
85. Bykov A M et al. *Mon. Not. R. Astron. Soc.* **453** 113 (2015)
86. Bykov A M et al. *Space Sci. Rev.* **214** 41 (2018)
87. Mészáros P *Rep. Prog. Phys.* **69** 2259 (2006)
88. Zhang B, Yan H *Astrophys. J.* **726** 90 (2011)
89. Bykov A et al. *Space Sci. Rev.* **173** 309 (2012)
90. MacFadyen A I, Woosley S E *Astrophys. J.* **524** 262 (1999)
91. McKinney J C, Blandford R D *Mon. Not. R. Astron. Soc.* **394** L126 (2009)
92. Bromberg O, Tchekhovskoy A *Mon. Not. R. Astron. Soc.* **456** 1739 (2016)
93. Senno N, Murase K, Mészáros P *Phys. Rev. D* **93** 083003 (2016)
94. Eichler D et al. *Nature* **340** 126 (1989)
95. Bromberg O et al. *Astrophys. J.* **764** 179 (2013)
96. Berger E *Annu. Rev. Astron. Astrophys.* **52** 43 (2014)
97. Blandford R D, Znajek R L *Mon. Not. R. Astron. Soc.* **179** 433 (1977)
98. Nomoto K *Int. J. Mod. Phys. D* **25** 1630025 (2016)
99. Abbott B P et al. *Astrophys. J. Lett.* **848** L13 (2017)
100. Savchenko V et al. *Astrophys. J. Lett.* **848** L15 (2017)
101. Abbott B P et al. (LIGO Sci. Collab. and Virgo Collab.) *Phys. Rev. Lett.* **119** 161101 (2017)
102. Rees M J *Nature* **333** 523 (1988)
103. Syrovatskii S I *Sov. Phys. Usp.* **14** 533 (1972); *Usp. Fiz. Nauk* **104** 669 (1971)
104. Syrovatskii S I *Sov. Phys. Usp.* **19** 354 (1976); *Usp. Fiz. Nauk* **118** 738 (1976)

105. Vainshtein S I, Bykov A M, Toptygin I N *Turbulence, Current Sheets, and Shocks in Cosmic Plasma* (Langhorne, Pa.: Gordon and Breach Sci. Publ., 1993)
106. Lyutikov M *Mon. Not. R. Astron. Soc.* **346** 540 (2003)
107. Hills J G *Nature* **254** 295 (1975)
108. Pfeffer D N, Kovetz E D, Kamionkowski M *Mon. Not. R. Astron. Soc.* **466** 2922 (2017)
109. Batista R A, Silk J *Phys. Rev. D* **96** 103003 (2017)
110. Senno N, Murase K, Mészáros P *Astrophys. J.* **838** 3 (2017)
111. Bloom J S et al. *Science* **333** 203 (2011)
112. Burrows D N et al. *Nature* **476** 421 (2011)
113. Berger E et al. *Astrophys. J.* **748** 36 (2012)
114. Khabibullin I, Sazonov S *Mon. Not. R. Astron. Soc.* **444** 1041 (2014)
115. Pavlinsky M et al. *Proc. SPIE* **9603** 96030C (2015)
116. Predehl P et al. *Proc. SPIE* **9905** 99051K (2016)
117. Acharya B S et al. *Astropart. Phys.* **43** 3 (2013)
118. De Angelis A et al. (e-ASTROGAM Collab.) *Exp. Astron.* **44** 25 (2017)
119. Bykov A M et al. *Tech. Phys.* **62** 819 (2017); *Zh. Tekh. Fiz.* **87** 803 (2017)
120. Moriya T J, Sorokina E I, Chevalier R A *Space Sci. Rev.* **214** 59 (2018)
121. Raymond J C *Space Sci. Rev.* **214** 28 (2018)
122. Margutti R et al. *Astrophys. J. Lett.* **856** L18 (2018)
123. Alexander K D et al. *Astrophys. J. Lett.* **863** L18 (2018); arXiv:1805.02870
124. Xie X, Zrake J, MacFadyen A *Astrophys. J. Lett.* **863** 58 (2018); arXiv:1804.09345
125. Lipunov V M, Postnov K A, Prokhorov M E *Astron. Rep.* **45** 236 (2001); *Astron. Zh.* **78** 276 (2001)
126. Lazzati D, Begelman M C *Astrophys. J.* **629** 903 (2005)
127. Gill R, Granot J *Mon. Not. R. Astron. Soc.* **478** 4128 (2018)
128. Côté B et al. *Astrophys. J.* **855** 99 (2018)